Check for updates

Thermoelectric properties of DO$_3$ V$_3$Al using first principles calculations

Xiaorui Chen, Yuhong Huang and Hong Chen [ID] *

The structural, electronic, and thermoelectric properties of DO$_3$ V$_3$Al in the paramagnetic (PM) and antiferromagnetic (AF) phases are investigated using the semi-classical Boltzmann theory in combination with deformation potential theory from first-principles calculations. The structural results are consistent with other theoretical and experimental data. AF-DO$_3$ V$_3$Al is verified to be a gapless semiconductor. Based on the calculated relaxation time τ and lattice thermal conductivity κ_L, the thermoelectric properties of PM-DO$_3$ and AF-DO$_3$ V$_3$Al have been predicted. Compared with PM-DO$_3$ V$_3$Al, the AF-DO$_3$ phase exhibits favorable thermoelectric performance. The optimized thermoelectric figure of merit ZT of the p-type AF-DO$_3$ phase can be as high as 0.32 at $T = 500$ K. It is possible to make V$_3$Al a promising candidate for efficient thermoelectricity by reducing its thermal conductivity.

1 Introduction

Thermoelectric (TE) materials can realize electric power generation from waste heat, thus they are considered as potential materials to be used to address both the energy crisis and environmental pollution. The performance of thermoelectric materials is measured according to a dimensionless figure of merit in the form of $ZT = S^2\sigma T/\kappa$. In the equation, S is the Seebeck coefficient, T denotes the absolute temperature, σ stands for the electrical conductivity and κ is the thermal conductivity. However, the thermal conductivity κ consists of the lattice thermal conductivity κ_L and electronic conductivity κ_e. The fact is that the higher the ZT value, the better the performance of a thermoelectric material is.[1] To obtain an ideal thermoelectric material, one must try to maximize the Seebeck coefficient S, maximize the electrical conductivity σ and minimize the thermal conductivity κ. Identifying and designing materials with high ZT has proven to be very challenging because of the mutual coupling among S, σ and κ.

Ternary Half-Heusler (HH) alloys such as MCoSb and MNiSn (M = Ti, Zr, and Hf) have great potential as high-temperature thermoelectric materials due to their high power factor (S^2).[2–5] These compounds, formed in a cubic crystal structure with an $F\bar{4}3m$ (no. 216) space group, are semiconductors with an 18 valence electron count (VEC) per unit cell, a narrow energy gap, and a Fermi level slightly above the top of the valence band, and so, they have a decent Seebeck coefficient with moderate electrical conductivity. ZT values of 0.8–1.0 for n-type half-Heusler alloys (Zr,Hf)NiSn have been achieved at 600–700 °C.[6,7] The studies on n-type Hf$_{0.5}$Zr$_{0.25}$NiSn$_{0.975}$Sb$_{0.025}$ (ref. 8) and p-type

Hf$_{0.5}$Zr$_{0.25}$CoSn$_{0.8}$Sb$_{0.2}$ (ref. 9) showed that the values of ZT can be improved to 1.0 and 0.8, respectively. From first-principles calculations, the thermoelectric properties of half-Heusler alloys ABPb (A = Hf,Zr; B=Ni,Pd) were also studied.[10] Fu and his collaborators obtained a maximum ZT of 1.1 in p-type FeNb$_{1-x}$Ti$_x$Sb ($0.04 \leq x \leq 0.24$)[11] at a temperature of 1100 K. Then, they focused their attention on the p-type FeNbSb crystal and reported that the value of ZT reached up to 1.5 at 1200 K.[12] However, the ZT values of HHs are still lower than those of most state-of-the-art thermoelectric materials. The search into the fundamentals and improvement in TE transport phenomena continues.

Recently, another Heusler-like alloy, DO$_3$ V$_3$Al, was theoretically anticipated to be an antiferromagnetic (AF) gapless semiconductor (GS),[13] and then was experimentally synthesized by arc-melting and annealing and characterized as a GS[14] with a zero magnetic moment. V$_3$Al exhibits many typical features of a good room-temperature TE material, such as a narrow band gap and a high density of states near the band edges. Understanding phonon and electron transport in V$_3$Al is important in the design and optimization of TE materials. In order to systematically study the relationship between the TE properties and the structural features and to understand the transport mechanisms in TE materials, we present a theoretical insight into the structural, electronic, and thermoelectric properties of DO$_3$ V$_3$Al by employing the semi-classical Boltzmann transport theory and deformation potential theory performed with first-principles calculations.

2 Computational method and process

We performed the electronic structure calculations of V$_3$Al by applying density function theory (DFT),[15,16] as implemented in

School of Physical Science and Technology, Southwest University, Chongqing 400715, China. E-mail: chenh@swu.edu.cn

RSC Advances Paper

the VASP package[17–19] according to the projector-augmented wave (PAW) method.[20] The generalized gradient approximation (GGA) with Perdew–Burke–Ernzerhof (PBE) functionals[21] is adopted to deal with the exchange-correlation energy. A Monkhorst–Pack k-mesh sample of $15 \times 15 \times 15$ in the whole Brillouin zone and a cut-off energy of 560 eV are used. The optimal structure is considered to be optimized when the force carried on each atom is less than 0.01 eV Å^{-1}. Transport calculations conducted rely on the semi-classic Boltzmann transport theory within the BoltzTrap code,[22] which has been successfully used to predict the performance of some thermoelectric (TE) materials.[23–25]

Theoretical treatments for both phonon and electron transport still have two challenges to be solved in order to get accurate predictions for TE materials. Firstly, many theoretical calculations on electrical conductivity κ_e are usually based on a constant relaxation time or a non-constant one from an experiment,[26,27] the reliability of which still remains to be confirmed in many cases. The relaxation time is usually very complicated since it depends on detailed scattering mechanisms. The lattice constant is quite small compared with the wavelength of thermally activated carriers at room temperature. Then, the scattering of carriers is dominated by the electron-acoustic phonon coupling.[28] Hence, the deformation potential (DP) theory together with the effective mass approximation is adopted to evaluate the relaxation time in this study. The relaxation time at temperature T for a three-dimensional system is[29]

$$\tau = \frac{2\sqrt{2}C\hbar^4}{3(k_B T m)^{3/2} E^2},$$ (1)

where C represents the elastic constant which takes the form of

$$C = \frac{1}{V_0}\frac{\partial^2 E}{\partial(\Delta l/l_0)^2},$$ (2)

in which V_0 and l_0 are the equilibrium volume and lattice parameter, $\Delta l = l - l_0$ which is the lattice distortion and E is the corresponding free energy of the system. The DP constant E denotes the shift of the conduction (valence) band edge with respect to unit strain, which can be defined as

$$E = \frac{\partial E_{edge}}{\partial(\Delta l/l_0)}.$$ (3)

The effective mass m at the conduction (valence) band edge is calculated from

$$m = \sqrt[3]{m_x^* m_y^* m_z^*},$$ (4)

where m_x^*, m_y^*, and m_z^* are the effective masses along the x, y and z directions, respectively. With f_0 standing for the equilibrium Fermi–Dirac distribution function, μ representing the chemical potential, and $\vec{v}_{\vec{k}}$ denoting the group velocity at state $\vec{k}$, the Seebeck coefficient S is in the form of

$$S = \frac{ek_B}{\sigma}\int d\varepsilon\left(-\frac{\partial f_0}{\partial \varepsilon}\right)\Xi(\varepsilon)\frac{\varepsilon - \mu}{k_B T},$$ (5)

in which the transport distribution function can be written as

$$\Xi(\varepsilon) = \sum \vec{v}_{\vec{k}}\vec{v}_{\vec{k}}\vec{\tau}_{\vec{k}}.$$ (6)

The electrical conductivity σ is given by

$$\sigma = e^2 \int d\varepsilon\left(-\frac{\partial f_0}{\partial \varepsilon}\right)\Xi(\varepsilon).$$ (7)

It is noted that the three mentioned parameters (C, E, and m) can be obtained from the DFT calculations. Thus, one can predict the relaxation time of different carriers. Secondly, the lattice thermal conductivity κ_L is considered to be in sum with the electronic component κ_e to obtain the thermal conductivity κ. We employ a simplified Debye–Callaway model[30] to calculate κ_L which contains acoustic and optical phonon modes. However, the acoustic phonon is usually dominant in κ_L and approximated to be[31]

$$\kappa_{L,ac} = \frac{(6\pi^2)^{2/3}}{4\pi^2}\frac{\bar{M}V_s^3}{TV^{2/3}\gamma^2 n^{1/3}},$$ (8)

in which $\bar{M}$ is the mass per atom in the crystal, V is the average volume of all the atoms, and n is the total atomic number in the primitive cell. We consider the Grüneisen parameter γ from the structural data as implemented within the quasi-harmonic Debye model.[32] The speed of sound V_s can be approximated using the formula $V_s \simeq \sqrt{B/d}$ with B and d respectively denoting the bulk modulus and density. The optical phonon modes can be described as[33]

$$\kappa_{L,op} = \frac{3k_B V_s}{2V^{2/3}}\left(\frac{\pi}{6}\right)^{1/3}\left(1 - \frac{1}{n^{2/3}}\right).$$ (9)

So far, we can get the magnitude of lattice thermal conductivity κ_L and it is possible to make a prediction of the ZT value.

3 Results and discussion

3.1 Structural property

The superconducting properties of pseudo-Heusler DO_3 structure V_3Al have been studied during the past few decades.[34–36] In addition, the antiferromagnetic (AF) gapless semiconducting DO_3 phase of V_3Al was successfully observed in experiment.[14] The space group of the DO_3 structure is $Fm\bar{3}m$, which is the same as that of the $L2_1$ structure. In general, the ternary $L2_1$ structure is represented by the generic formula X_2YZ. When the Y element is replaced by X, it turns out to be the binary DO_3 structure with X_3Z basis. So, the Al atom in V_3Al is located at the 4a (0,0,0) position of Wyckoff coordination. The two inequivalent V atoms respectively occupy the 4b (0.5,0.5,0.5) (labeled V_1) and 4c (0.25,0.25,0.25) (labeled V_2) positions,[37] as shown in Fig. 1. It is noted that both the V_2 atoms are equal in the paramagnetic (PM) phase, but in the AF phase they possess opposite spin directions as can be seen in Fig. 1. From the DFT calculation, the V_2 atoms of the AF phase hold anti-aligned moments of 1.527 μ_B per atom and the V_1 atom remains nonmagnetic. Fig. 2(a) presents the total energy of PM-DO_3 and
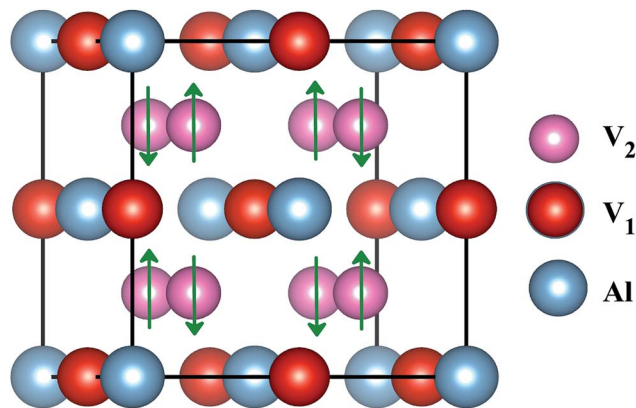
Fig. 1 The structure of antiferromagnetic DO_3-V_3Al. The up and down arrows stand for the positive and negative spins of the V_2 atoms.

Table 1 The calculated deformation potential constant E, elastic constant C, effective mass m and obtained relaxation time τ at room temperature of PM-DO_3 and AF-DO_3 V_3Al

Phase	Carrier type	E (eV)	C	m (m_e)	τ (f_s)
PM-DO_3	Electron	28.89	1.67	0.04	742
	Hole	28.89	1.67	0.07	403
AF-DO_3	Electron	28.92	1.45	0.05	493
	Hole	28.92	1.45	0.08	273

AF-DO_3 V_3Al as the variation of lattice parameter l relative to equilibrium lattice parameter l_0 ranges from -0.05 to 0.05. The calculated results are expressed by dots and the solid lines are the fitted data using the Murnaghan equation of state.[38,39] The obtained elastic constant C values for both the PM-DO_3 and AF-DO_3 phases are listed in Table 1. It is noted that the total energy of the AF-DO_3 V_3Al is much smaller than that of the PM-DO_3 phase. As a result, we confirm the metastability of PM-DO_3 V_3Al. The optimized lattice parameter in this study is 6.067 Å, which is similar to the value of 6.06 Å from another theoretical result.[13]

3.2 Electronic structure

Now, we focus on the density of states and band structure of PM-DO_3 and AF-DO_3 V_3Al. From Fig. 3(a), it can be seen that

both the top of the valence band and the bottom of the conduction band are sited at point W and they just touch together, thus a band gap does not exist. There are also some states in Fig. 3(b) around the Fermi level. As a result, PM-DO_3 V_3Al is a metal. It is also seen that the local DOS (LDOS) of the V_1 with V_2 atoms contributes to the major total DOS. In order to further explore the bonding features, the projected DOSs (PDOSs) for the s-, p-, and d-orbitals of the V_1 and V_2 atoms are drawn in Fig. 3(c and d). The d-orbitals of the two V atoms dominate the LDOS, showing the d–d hybridization between the V_1–V_2 atoms for PM-DO_3 V_3Al. However, the total DOS of AF-DO_3 V_3Al in two spin directions is symmetrical, as shown in Fig. 3(f). In the AF configuration shown in Fig. 3(e), the maximum of the valence band and the minimum of the conduction band are quite close, thus forming a small direct band gap, which is the same as in other theoretical studies,[14,40] and the band gap is smaller than 0.1 eV. AF-DO_3 V_3Al therefore exists as an anti-ferromagnetic gapless semiconductor.[14] The LDOSs of the V_1 and V_2 atoms contribute mostly to AF-DO_3 V_3Al's total DOS. From Fig. 3(g) and (h), it can be seen that the bonding
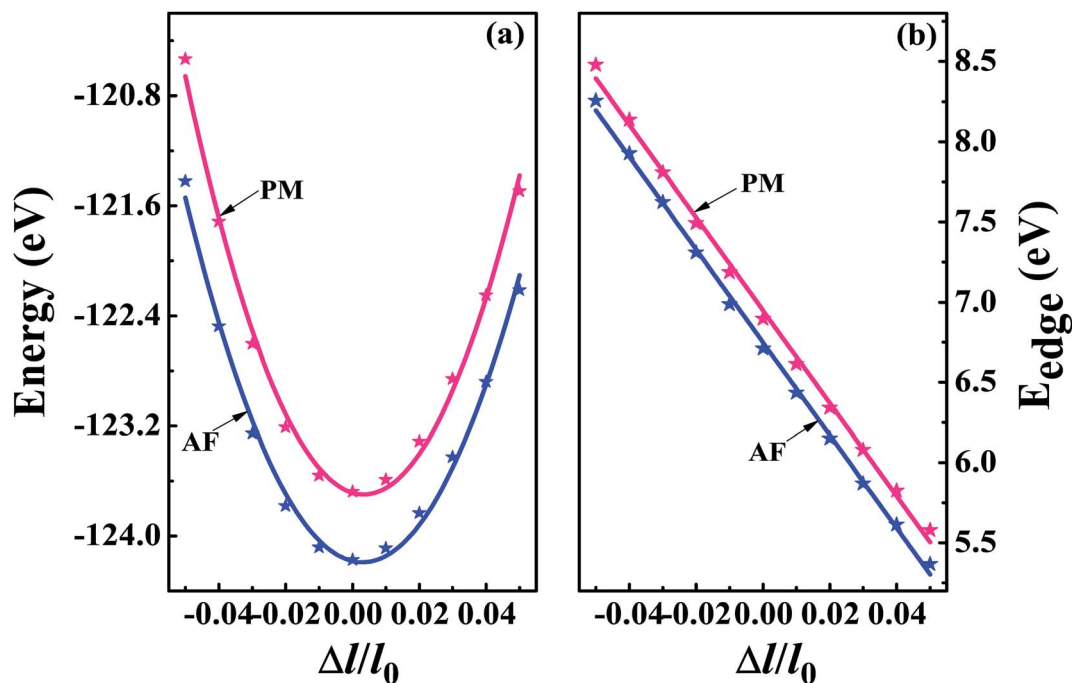

Fig. 2 The total energy (a) and band edge energy (E_{edge}) (b) *versus* the uniaxial strain $\Delta l/l_0$ with $\Delta l = l - l_0$ and l_0 denoting the equilibrium lattice parameter. The calculated results are expressed by dots and the solid lines are the fitted data for both PM-DO_3 V_3Al (shown in red) and AF-DO_3 V_3Al (shown in blue).
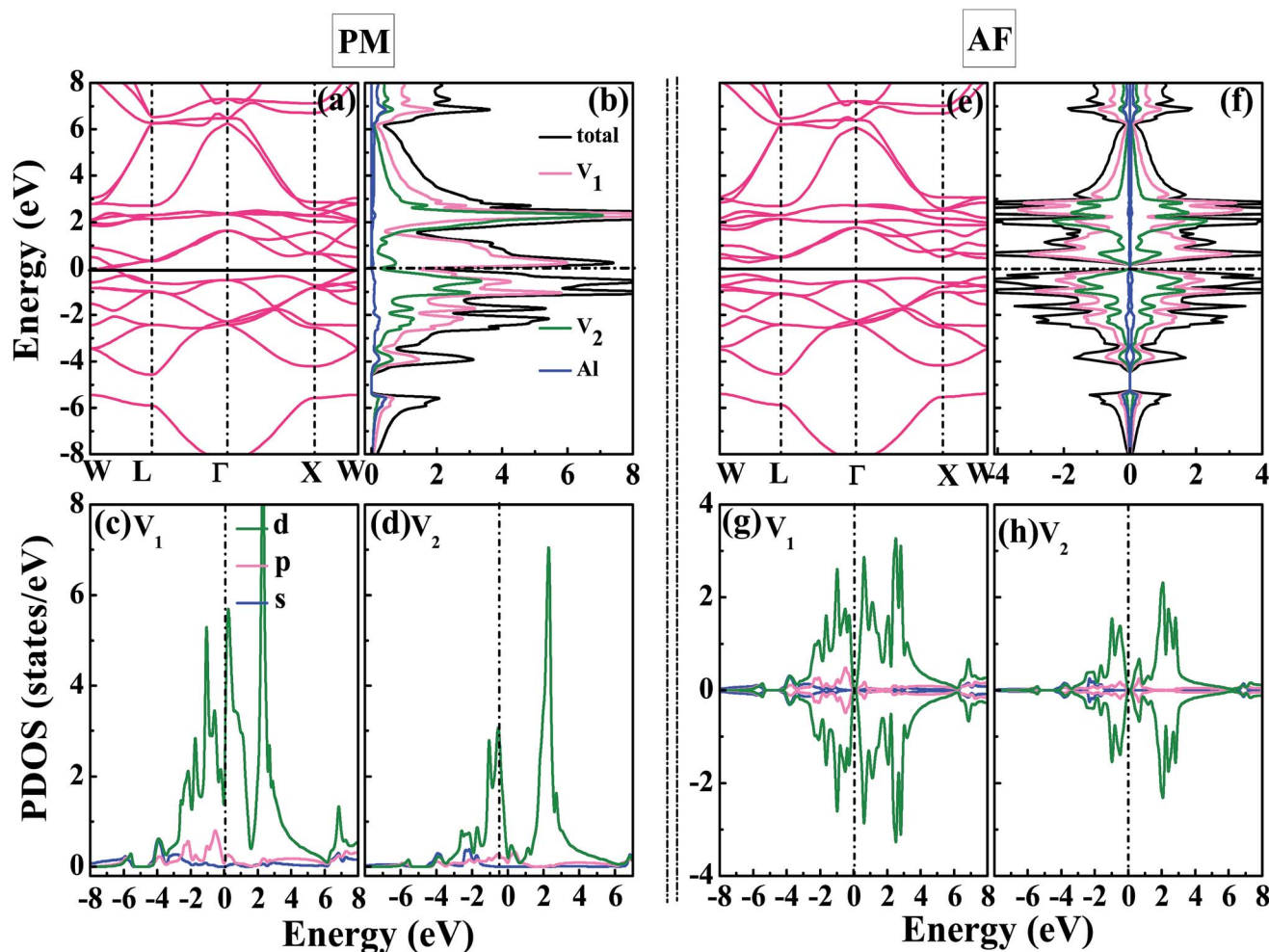
Fig. 3 The calculated band structure (a), total DOS for V_3Al together with local DOSs (LDOSs) for the V_1 atoms, V_2 atoms, and Al atoms (b), projected DOSs (PDOSs) for the s-, p-, and d-orbitals of the V_1 atoms (c), together with those of the V_2 atoms (d) for PM-DO_3 V_3Al. The calculated band structure (e), total DOS and LDOSs (f), PDOSs of V_1 (g), together with the PDOSs of V_2 (h) for AF-DO_3 V_3Al. The dashed lines in the DOSs denote the Fermi levels.

characteristics in the AF-DO_3 phase are preserved and the same as in the case of PM-DO_3. It is the hybridization of the V_1 and V_2 d-bands that makes the main contribution of the total DOS.

On the other hand, we obtain the effective mass m for both the n-type and p-type carriers of PM-DO_3 and AF-DO_3 V_3Al from the above electronic structure calculation and list in Table 1. The valence band maximum (VBM) touches the conduction band minimum (CBM) for both phases of V_3Al, so the energy values of the VBM and CBM are the same. Fig. 2(b) plots this same band edge energy (E_{edge}) *versus* the ratio of lattice distortion $\Delta l = l - l_0$ and equilibrium lattice parameter l_0 for PM-DO_3 and AF-DO_3 V_3Al. They exhibit good linear dependence and the E_{edge} of AF-DO_3 V_3Al is a little lower than that of the PM-DO_3 phase. Here, we obtain DP constant values, as summarized in Table 1, together with the elastic constant C, effective mass m and relaxation time τ at room temperature for electrons and holes of PM-DO_3 and AF-DO_3 V_3Al. The effective mass m next to the CBM of PM-DO_3 V_3Al is about 0.04 m_e, which is smaller than the 0.07 m_e near the VBM. This is due to the fact that the energy

band next to the CBM is sharper than that next to the VBM. Similarly, for AF-DO_3 V_3Al, the sharper energy band near the CBM also results in a smaller effective mass. As a result, the relaxation time for holes is shorter than that for electrons in both PM-DO_3 and AF-DO_3 V_3Al. It is noted that the relaxation time between two carriers is also obviously different in other systems such as NbFeSb[41] and LaPtSb.[42] Otherwise, the relaxation time of electrons and holes in V_3Al is much larger than that in thermoelectric materials like ZrNiPb,[43] suggesting the promising thermoelectric performance of V_3Al.

3.3 Thermoelectric properties

Fig. 4(a) shows the lattice thermal conductivity κ_L as a function of temperature for V_3Al. The acoustic phonon lattice thermal conductivity $\kappa_{L,ac}$ and optical phonon mode $\kappa_{L,op}$ in the temperature range from 0 to 1200 K are plotted in Fig. 4(b) and (c), respectively. It is seen that the total κ_L is dominated by $\kappa_{L,ac}$ and $\kappa_{L,op}$ makes very little contribution to κ_L. On the other hand, both the components of AF-DO_3 V_3Al are smaller than those of
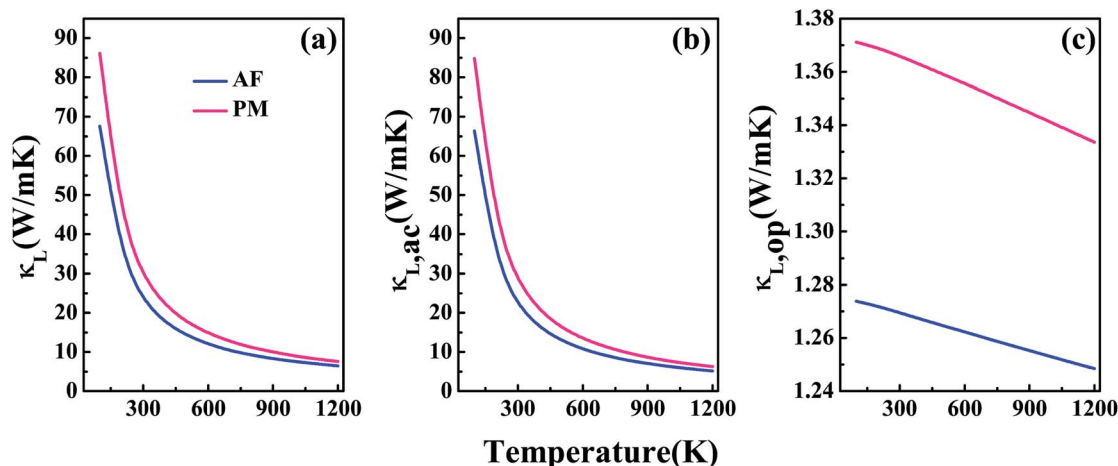
Fig. 4 The calculated lattice thermal conductivity κ_L (a) and its two components: acoustic phonon modes $\kappa_{L,ac}$ (b) and optical phonon modes $\kappa_{L,op}$ (c).

PM-DO$_3$ V$_3$Al. Therefore, the former phase has a lower value of total κ_L. It is important to note that such a lower κ_L value may suggest the favorable TE performance of AF-DO$_3$ V$_3$Al compared to the other phase.

Now we have obtained all of the transport coefficients (including the Seebeck coefficient S, the electronic conductivity σ and the total thermal conductivity κ) for PM-DO$_3$ and AF-DO$_3$ V$_3$Al. By inserting them into the formula $ZT = S^2\sigma T/\kappa$, one can
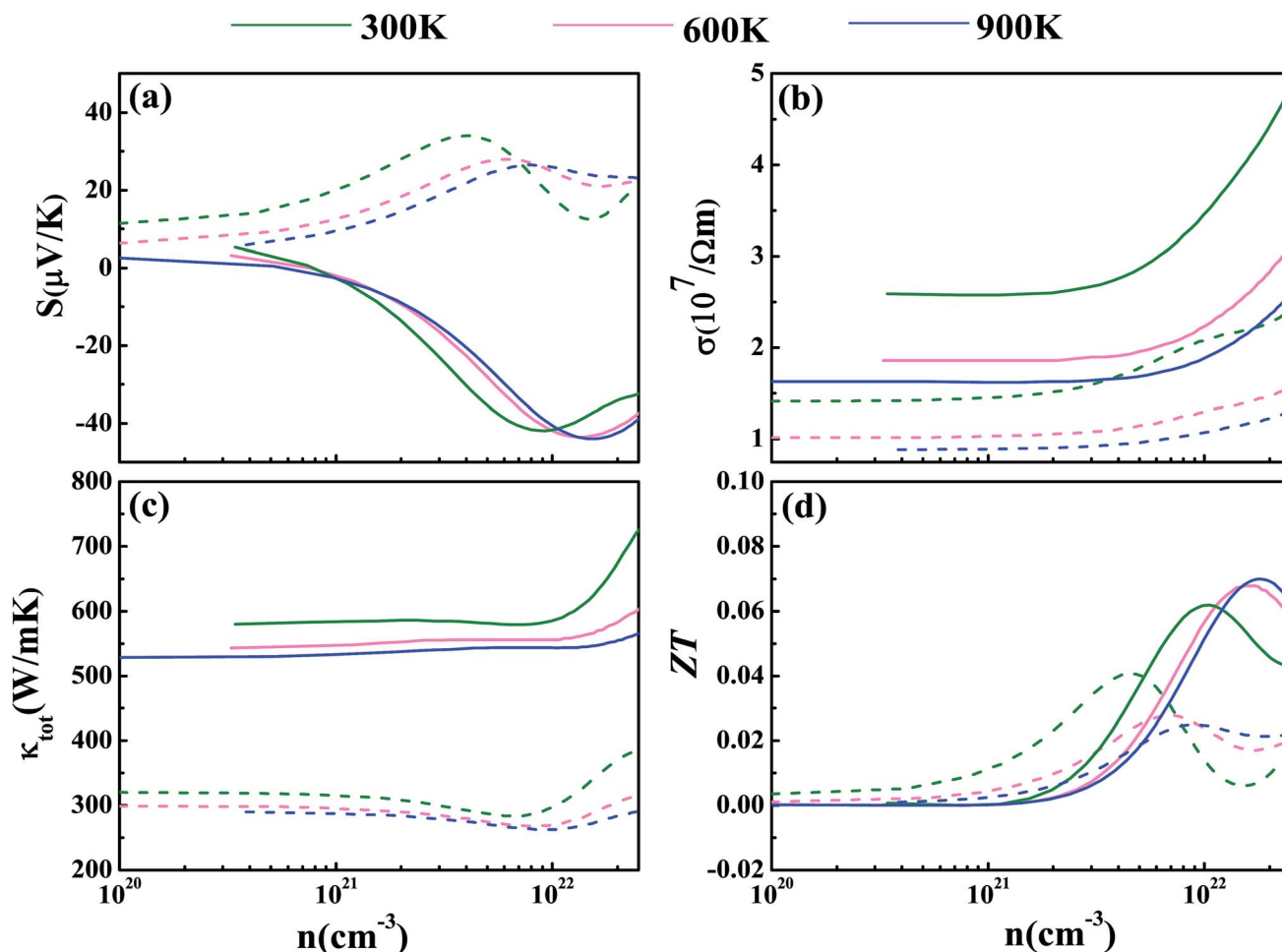

Fig. 5 The calculated Seebeck coefficient S (a), electronic conductivity σ (b), total thermal conductivity κ_{tot} (c), and thermoelectric figure of merit ZT (d) at $T = 300$ K (shown in green), 600 K (shown in pink), and 900 K (shown in blue) for PM-DO$_3$ V$_3$Al. The dashed and solid lines represent the p-type and n-type phases, respectively.

get useful information about the thermoelectric performance. In Fig. 5 and 6, we summarize some representative sets of data about these coefficients as a function of carrier concentration n respectively for PM-DO$_3$ and AF-DO$_3$ V$_3$Al when the temperature is 300 K, 600 K and 900 K. The TE performances of n-type V$_3$Al are shown by solid lines and dashed lines show those of p-type V$_3$Al. The absolute value of S firstly increases and then decreases as n increases at a constant temperature. This value is larger at lower temperature before the single-peaked value and the Seebeck coefficient S at higher temperature holds a larger value when the carrier concentration grows further. It also can be seen that the absolute value of S for AF-DO$_3$ V$_3$Al is greater than that of PM-DO$_3$ V$_3$Al, thus predicting the favorable thermoelectric performance of AF-DO$_3$ V$_3$Al. The electrical conductivity σ of n-type V$_3$Al is higher than that of p-type V$_3$Al for both phases which results from the significant difference between the relaxation times of the two different carriers. Fig. 5(b) shows that the magnitude of σ is sensitive to temperature in the whole mentioned carrier concentration, but the σ value is insensitive to T before the carrier concentration reaches 10^{21} cm^{-3}. We can see from Fig. 5(a) and (b) that there exists an obvious increasing trend of σ at the carrier concentration where the absolute value

of S is very small, which is similar to that found in Fig. 6(a) and (b). So it is of great importance to find a good balance between the Seebeck coefficient and electrical conductivity for V$_3$Al. By adding the calculated lattice thermal conductivity κ_L to the obtained electronic thermal conductivity κ_e, we get the total thermal conductivity κ_{tot}. κ_{tot} exhibits the same dependency on carrier concentration as σ shows when the temperature remains unvaried. Nevertheless, the total κ appears to exhibit an increasing trend with increasing temperature in the low n ranges for AF-DO$_3$ V$_3$Al as shown in Fig. 6(c). Finally, we are able to evaluate the thermoelectric performance of V$_3$Al. As shown in Fig. 5(d), the obtained ZT value of n-type PM-DO$_3$ V$_3$Al is rather larger than that of p-type PM-DO$_3$ V$_3$Al and the ZT data for both are unfortunately quite low for this phase of V$_3$Al. For AF-DO$_3$ V$_3$Al, the ZT is greatly enhanced as seen in Fig. 6(d). A large ZT of 0.297 for the n-type system is obtained at the optimal conditions ($n = 1.39 \times 10^{22}$ cm^{-3} and $T = 600$ K). For the p-type system, at $n = 2.31 \times 10^{22}$ cm^{-3} and $T = 600$ K, the ZT reaches 0.319. As temperature keeps increasing, the peak height of both maximal ZT values firstly increases and then decreases with the increasing carrier concentration. In order to further explore the temperature influence on the ZT of AF-DO$_3$ V$_3$Al, we plot Fig. 7.
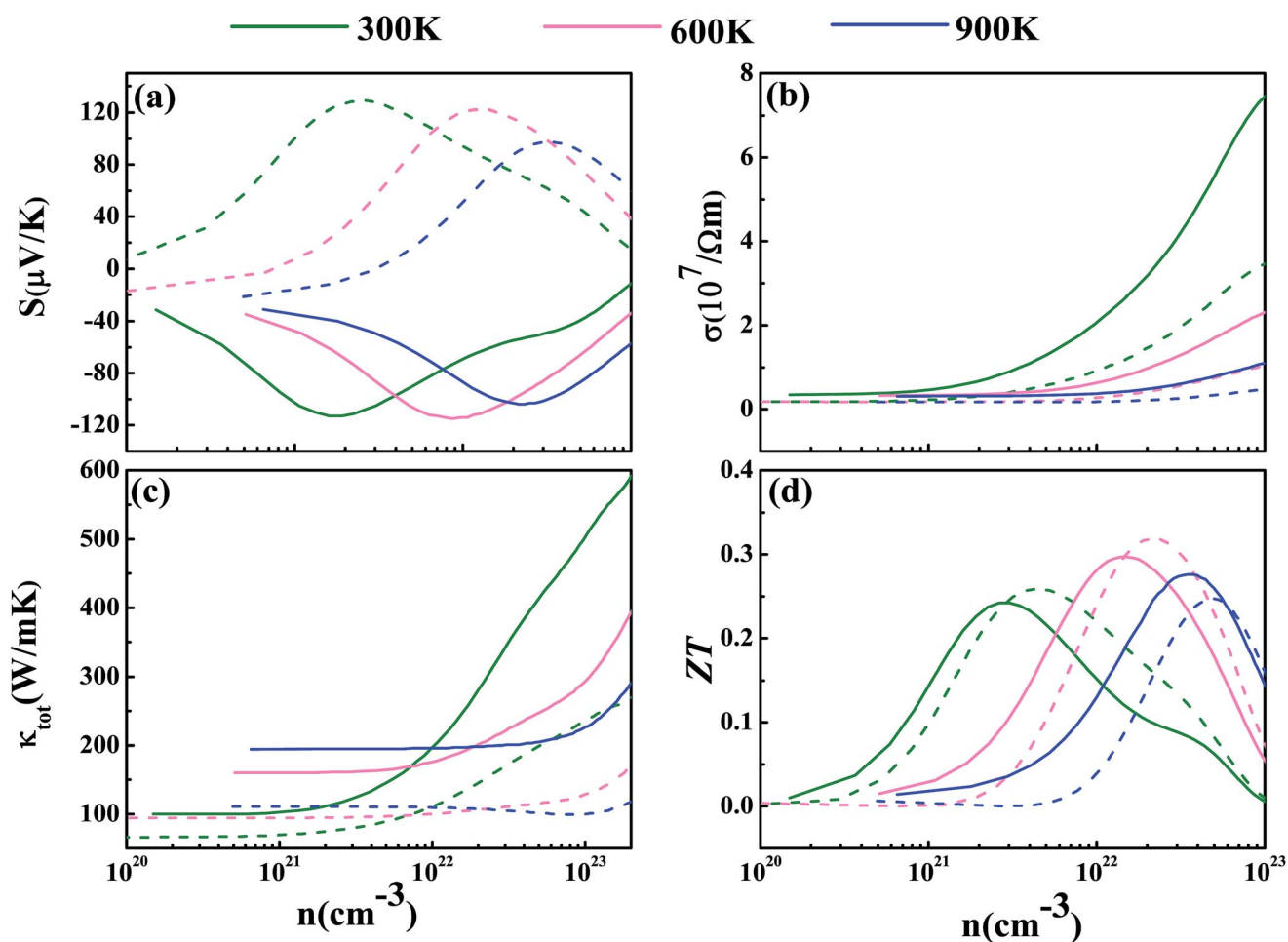

Fig. 6 The calculated Seebeck coefficient S (a), electronic conductivity σ (b), total thermal conductivity κ_{tot} (c), and thermoelectric figure of merit ZT (d) at $T = 300$ K (shown in green), 600 K (shown in pink), and 900 K (shown in blue) for AF–DO$_3$ V$_3$Al. The dashed and solid lines represent the p–type and n–type phases, respectively.
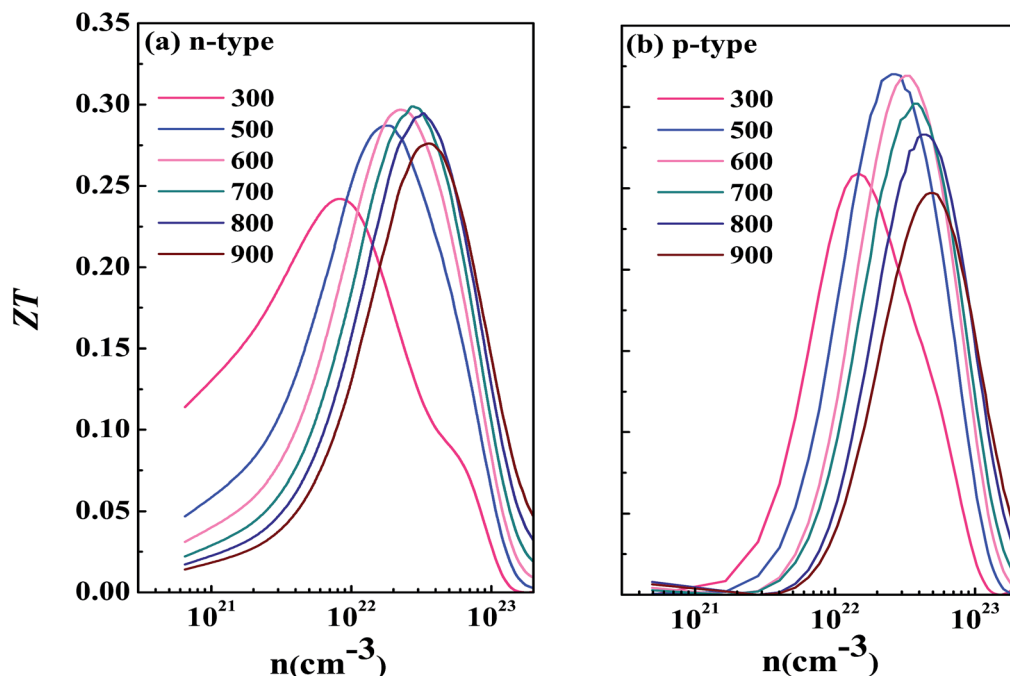
Fig. 7 The calculated ZT as a function of temperature for n-type AF–DO$_3$ V$_3$Al (a) and p-type AF–DO$_3$ V$_3$Al (b).

The maximal ZT of n-type AF-DO$_3$ V$_3$Al appears to be 0.3 when n and T are respectively tuned to 2.05×10^{22} cm^{-3} and 700 K. For the p-type AF-DO$_3$ V$_3$Al, the optimal ZT data is further enhanced to be 0.32 at a concentration of 1.59×10^{22} cm^{-3} and temperature of 500 K. The calculated upper limit ZT values of XNiSn (X = Hf, Zr, and Ti) are severally 0.22, 0.26, and 0.29 and it is 0.30 for ZrNiPb,[43] which are all less than that of p-type AF-DO$_3$ V$_3$Al, thus suggesting the better TE performance of p-type AF-DO$_3$ V$_3$Al. However, there are still many TE materials like ZrRhBi,[44] FeNbSb,[45] and Nb$_{1-x}$Ti$_x$FeSb alloys[41] which show favorable thermoelectric performances. Compared with the transport coefficients (S, σ, and κ) of all the just mentioned TE materials, V$_3$Al is found to have a high thermal conductivity κ, which is a fatal disadvantage in obtaining a high ZT value. So, reducing the magnitude of the thermal conductivity κ may be an effective approach to attain better TE performance.

4 Conclusions

The structural, electronic, and thermoelectric properties of PM-DO$_3$ V$_3$Al and AF-DO$_3$ V$_3$Al have been systematically studied by employing first-principles calculations based on DFT theory. By calculating the total energy *versus* volume, it is found that V$_3$Al prefers to be an antiferromagnetic system. The obtained equilibrium lattice constant is 6.067 Å, which is similar to other theoretical results. Electronic structure calculations confirm the gapless semiconductor properties of antiferromagnetic V$_3$Al. In order to understand the thermoelectric properties of V$_3$Al, we firstly obtained the relaxation time τ using deformation potential theory and the lattice thermal conductivity κ_L from the DFT results. The values of κ_L for PM-DO$_3$ V$_3$Al and AF-DO$_3$ V$_3$Al are respectively 29.16 W mK^{-1} and 23.14 W mK^{-1} at room temperature. Then the Seebeck coefficient S, electrical conductivity κ, thermal conductivity σ, and ZT values of both phases of V$_3$Al were investigated. PM-DO$_3$ V$_3$Al exhibits a lower Seebeck coefficient, resulting in a worse thermoelectric performance. The maximal ZT value of p-type AF-DO$_3$ V$_3$Al reaches 0.32 at $n = 1.59 \times 10^{22}$ cm^{-3} and $T = 500$ K. Further studies should be focused on reducing the thermal conductivity to enhance the TE performance of AF-DO$_3$ gapless semiconductor V$_3$Al. We hope that our calculations and results offer useful guidance for further study on TE materials.

Conflicts of interest

There are no conflicts to declare.

Acknowledgements

References

1 Y. Ma, R. Heijl and A. E. C. Palmqvist, *J. Mater. Sci.*, 2013, **48**, 2767–2778.
2 H. Hohl, A. P. Ramirez, C. Goldmann, G. Ernst, B. Wölfing and E. Bucher, *J. Phys.: Condens. Matter*, 1999, **11**, 1697–1709.
3 G. S. Nolas, J. Poon and M. Kanatzidis, *MRS Bull.*, 2006, **31**, 199–205.

4   C. Yu, T. J. Zhu, R. Z. Shi, Y. Zhang, X. B. Zhao and J. He, *Acta Mater.*, 2009, **57**, 2757–2764.

5   Q. Shen, L. Chen, T. Goto, T. Hirai, J. Yang, G. P. Meisner and C. Uher, *Appl. Phys. Lett.*, 2001, **79**, 4165–4167.

6   G. Joshi, X. Yan, H. Z. Wang, W. S. Liu, G. Chen and Z. F. Ren, *Adv. Energy Mater.*, 2011, **1**, 643–647.

7   S. Populoh, M. H. Aguirre, O. C. Brunko, K. Galazka, Y. Lu and A. Weidenkaff, *Scr. Mater.*, 2012, **66**, 1073–1076.

8   S. R. Culp, S. J. P. N. Hickman, T. M. Tritt and J. Blumm, *Appl. Phys. Lett.*, 2006, **88**, 042106.

9   S. R. Culp, J. W. Simonson, S. J. Poon, V. Ponnambalam, J. Edwards and T. M. Tritt, *Appl. Phys. Lett.*, 2008, **93**, 022105.

10 G. T. Wang and D. Y. Wang, *J. Alloys Compd.*, 2016, **682**, 375–380.

11 C. G. Fu, T. J. Zhu, Y. T. Liu, H. H. Xie and X. B. Zhao, *Energy Environ. Sci.*, 2014, **8**, 216–220.

12 C. G. Fu, S. Q. Bai, Y. T. Liu, Y. S. Tang, L. D. Chen, X. B. Zhao and T. J. Zhu, *Nat. Commun.*, 2015, **6**, 9144.

13 G. Y. Gao and K. L. Yao, *Appl. Phys. Lett.*, 2013, **103**, 232409.

14 M. E. Jamer, B. A. Assaf, G. E. Sterbinsky, D. Arena, L. H. Lewis, A. A. Saúl, G. Radtke and D. Heiman, *Phys. Rev. B: Condens. Matter Mater. Phys.*, 2015, **91**, 094409.

15 P. Hohenberg and W. Kohn, *Phys. Rev.*, 1964, **136**, B864–B871.

16 W. Kohn and L. J. Sham, *Phys. Rev.*, 1965, **140**, A1133–A1138.

17 G. Kresse and J. Hafner, *Phys. Rev. B: Condens. Matter Mater. Phys.*, 1993, **47**, 558–561.

18 G. Kresse and J. Hafner, *Phys. Rev. B: Condens. Matter Mater. Phys.*, 1994, **49**, 14251–14269.

19 G. Kresse and J. Furthmüller, *Comput. Mater. Sci.*, 1996, **6**, 15–50.

20 P. E. Blöchl, *Phys. Rev. B: Condens. Matter Mater. Phys.*, 1994, **50**, 17953–17979.

21 J. P. Perdew, K. Burke and M. Ernzerhof, *Phys. Rev. Lett.*, 1996, **77**, 3865–3868.

22 G. K. H. Madsen and D. J. Singh, *Comput. Phys. Commun.*, 2006, **175**, 67–71.

23 B. L. Huang and M. Kaviany, *Phys. Rev. B: Condens. Matter Mater. Phys.*, 2008, **77**, 125209.

24 L. Q. Xu, Y. P. Zheng and J. C. Zheng, *Phys. Rev. B: Condens. Matter Mater. Phys.*, 2010, **82**, 195102.

25 J. J. Pulikkotil, D. J. Singh, S. Auluck, M. Saravanan, D. K. Misra, A. Dhar and R. C. Budhani, *Phys. Rev. B: Condens. Matter Mater. Phys.*, 2012, **86**, 155204.

26 A. J. Hong, L. Li, H. X. Zhu, Z. B. Yan, J. M. Liu and Z. F. Ren, *J. Mater. Chem. A*, 2015, **3**, 13365–13370.

27 V. K. Gudelli, V. Kanchana, G. Vaitheeswaran, A. Svane and N. E. Christensen, *J. Appl. Phys.*, 2013, **114**, 223707.

28 Y. Q. Cai, G. Zhang and Y. W. Zhang, *J. Am. Chem. Soc.*, 2014, **136**, 6269–6275.

29 J. Bardeen and W. Shockley, *Phys. Rev.*, 1950, **80**, 72–80.

30 J. Callaway, *Phys. Rev.*, 1959, **113**, 1046–1051.

31 E. S. Toberer, A. Zevalkink and G. J. Snyder, *J. Mater. Chem.*, 2011, **21**, 15843–15852.

32 E. Francisco, J. M. Recio, M. A. Blanco, A. M. Pendás and A. Costales, *J. Phys. Chem. A*, 1998, **102**, 1595–1601.

33 J. Yan, P. Gorai, B. Ortiz, S. Miller, S. A. Barnett, T. Mason, V. Stevanović and E. S. Toberer, *Energy Environ. Sci.*, 2015, **8**, 983–994.

34 Y. Du, G. Z. Xu, X. M. Zhang, Z. Y. Liu, S. Y. Yu, E. K. Liu, W. H. Wang and G. H. Wu, *Europhys. Lett.*, 2013, **103**, 37011.

35 L. R. Testardi, T. Wakiyama and W. A. Royer, *J. Appl. Phys.*, 1977, **48**, 2055–2061.

36 S. Ohshima, H. Ishida, T. Wakiyama and K. Okuyama, *Jpn. J. Appl. Phys*, 1989, **28**, 1362–1366.

37 A. Bansil, S. Kaprzyk, P. E. Mijnarends and J. Tobola, *Phys. Rev. B: Condens. Matter Mater. Phys.*, 1999, **60**, 13396–13412.

38 F. D. Murnaghan, *Proc. Natl. Acad. Sci. U. S. A.*, 1944, **30**, 244–247.

39 F. Birch, *Phys. Rev.*, 1947, **71**, 809–824.

40 I. Galanakis, Ş. Tırpancı, K. Özdoğan and E. Şaşıoğlu, *Phys. Rev. B*, 2016, **94**, 064401.

41 A. J. Hong, L. Li, R. He, J. J. Gong, Z. B. Yan, K. F. Wang, J. M. Liu and Z. F. Ren, *Sci. Rep.*, 2016, **6**, 22778.

42 Q. Y. Xue, H. J. Liu, D. D. Fan, L. Cheng, B. Y. Zhao and J. Shi, *Phys. Chem. Chem. Phys.*, 2016, **18**, 17912–17916.

43 S. D. Guo, *RSC Adv.*, 2016, **6**, 47953–47958.

44 Vikram, J. Kangsabanik, Enamullah and A. Alam, *J. Mater. Chem. A*, 2017, **5**, 6131–6139.

45 W. F. Li, G. Yang and J. W. Zhang, *J. Phys. D: Appl. Phys.*, 2016, **49**, 195601.